ChemPubSoc Europe

DOI: 10.1002/chem.201704822

CHEMISTRY
A European Journal
Full Paper

Magnetic Properties

Correlation of Structural and Magnetic Properties in a Set of Mononuclear Lanthanide Complexes

Peter Comba,*[a, b] Lena J. Daumann,[c] Rüdiger Klingeler,[d, e] Changhyun Koo,[d] Mark J. Riley,[f] Asha E. Roberts,[a, b] Hubert Wadepohl,[a] and Johannes Werner[d]

Abstract: The electronic and magnetic properties of a set of mononuclear terbium(III) and dysprosium(III) complexes with two tetradentate 1-hydroxy-pyridin-2-one (1,2-HOPO) ligands are reported. Two primary coordination geometries are observed, depending on the length of the linker between the 1,2-HOPO donor moieties and the resulting arrangements of the linker. Fine details of the magnetic circular dichroism (MCD) spectra of the dysprosium(III) complexes illustrate differences in the splitting of the *J* multiplets and allow for a thorough ligand field analysis. High frequency electron paramagnetic resonance (HF-EPR) studies of the terbium(III) complexes give insight into the composition of the ground states. Ab initio calculations are utilized to rationalize the experimental results and further illustrate the effect of the structural features on the electronic and magnetic properties of the different complexes.

Introduction

After the reported observation of magnetic hysteresis in Mn_{12}-acetate in 1993,[1] research in the area of single molecule magnets (SMMs) has flourished. With significant and ever increasing spin relaxation barriers, SMMs have attracted attention not purely out of fundamental interest, but also due to the diverse range of potential applications.[2] Since the relation between spin and magnetic anisotropy was established, lanthanides have taken center stage in the field of SMMs.[3]

Large spin-orbit coupling and strong anisotropy, leading to large magnetic moments and high spin reversal barriers, make many lanthanide-based complexes better candidates in this field than transition metal complexes.[4] Most notably, a recent leap of the record magnetic blocking temperature from 20 K[4c] to 60 K has been observed in a highly axial dysprosium metallocene complex, with a barrier of 1277 cm^{-1} (1837 K) in zero field.[4a,b]

The magnetic properties of SMMs are related to the electronic structure of the metal site and therefore to the molecular structure. For the prediction and interpretation of such properties it is common to utilize a well-established ab initio method.[5] This has become a standard procedure, although it is not without criticism.[6] Apart from magnetic studies, which only provide for qualitative/semi-quantitative correlations, rigorous validation of these computational methods is rarely reported. This paper serves as a continuation of our previous studies, in which we have utilized several spectroscopic and magnetometric techniques to validate our computational data.[7] We have reported both homodinuclear lanthanide(III) and heterodinuclear 3d–4f systems, combining our computed values with alternating and direct current (ac and dc) SQUID, high frequency EPR (HF-EPR), and magnetic circular dichroism (MCD) data, including extensive ligand field analysis based on angular overlap model (AOM) calculations.[7b,c] More recently we have utilized paramagnetic NMR spectroscopy and SQUID measurements to determine the solution and solid-state magnetic behavior of a series of linear trinuclear $Ni^{II}_2Ln^{III}$ complexes with Ln = Y, La, Ce, Nd, Sm, Eu, Gd, Tb, Dy, Ho, Er, Tm, Lu.[7a] Additionally, single crystal dc SQUID and HF-EPR data of the Ln = Dy complex has provided further validation of our ab initio calculated data.[8]

In the present study we have used both ab initio quantum chemical and experimental methods to investigate the ligand field effects on a set of octacoordinate mononuclear Ln^{III} complexes (Ln^{III} = Tb^{III} and Dy^{III}). We employ a selection of homoleptic ligands from a published series known as the LI-series (see

[a] Prof. P. Comba, A. E. Roberts, Prof. H. Wadepohl
Anorganisch-Chemisches Institut
Universität Heidelberg, INF 270, 69120 Heidelberg (Germany)
E-mail: peter.comba@aci.uni-heidelberg.de

[b] Prof. P. Comba, A. E. Roberts
Interdisziplinäres Zentrum für Wissenschaftliches Rechnen (IWR)
INF 205, 69120 Heidelberg (Germany)

[c] Prof. L. J. Daumann
Fakultät für Chemie und Pharmazie
Ludwig-Maximilians-Universität München
Butenandtstr. 5–13, 81377 Munich (Germany)

[d] Prof. R. Klingeler, Dr. C. Koo, J. Werner
Kirchhoff-Institut für Physik, Universität Heidelberg
INF 227, 69120 Heidelberg (Germany)

[e] Prof. R. Klingeler
Centre for Advanced Materials (CAM), Universität Heidelberg
INF 225, 69120 Heidelberg (Germany)

[f] Prof. M. J. Riley
School of Chemistry and Molecular Biosciences
University of Queensland, Brisbane, Queensland 4072 (Australia)

Supporting information and the ORCID identification number(s) for the author(s) of this article can be found under:
https://doi.org/10.1002/chem.201704822.

Figure 1).[9] The ligands are comprised of two bidentate donors (1-hydroxy-pyridin-2-one, 1,2-HOPO) with a linking backbone. Two ligands per metal ion result in octacoordinate complexes of only oxygen donors and, depending on the identity of the linker, different geometries at the Ln^{III} center are observed.

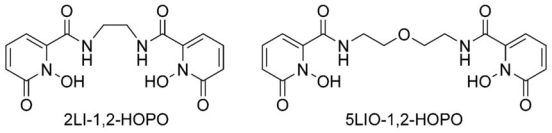

Figure 1. Ligands used in this study to form $Ln^{III}L_2$ complexes (Ln^{III} = Tb^{III} and Dy^{III}). The nomenclature *n*LI*m* is such that *n* indicates the number of atoms in the linking chain, and *m* indicates additional features on the chain.

Two primary binding modes exist for these ligands, the classification of which is based on the location of the linker in reference to a perfect triangular dodecahedron (Figure 3 below).[9a,10] While the 1,2-HOPO chelators will be positioned along the *m*-edges of the triangular dodecahedron, the bridges may occupy the *a*-edges (bridge is stretched) or the *g*-edges (bridge is folded).[10] Within these modes there are different symmetries, that is, S_4 or D_2 for *a*-edged, and *cis* or *trans* for *g*-edged. DFT optimizations and solid-state structures have shown that shorter bridges (two to four atoms) tend to favor the *a*-edged mode. Longer bridges (five to eight atoms) favor the *g*-edged mode, with *trans* symmetry preferred over *cis* due to steric interactions.[9a] Previously, the ligands have been investigated for their luminescent properties with Eu^{III} and Sm^{III}.[9] The imposed geometry of the ligands in these complexes was shown to have a significant impact on quantum yields. In the present study, we investigate the LI-series for their ligand field effects. In the interest of simplicity, only two ligands were selected for this purpose with chain lengths of two and five atoms (Figure 1).

Results and Discussion

Syntheses and structural properties

Syntheses of the ligands and mononuclear Ln^{III} complexes were carried out as reported elsewhere.[9] The respective ligand (2.5 equiv.), trichloride hexahydrate lanthanide salt (1 equiv.), and pyridine as a base were heated to reflux in methanol for 24 hours. Characterization by mass spectrometry and elemental analysis was carried out for all complexes. X-ray quality crystals were obtained for $[Tb^{III}(2LI\text{-}1,2\text{-}HOPO)_2]PyH$ (Tb^{III}-2LI) and $[Dy^{III}(2LI\text{-}1,2\text{-}HOPO)_2]PyH$ (Dy^{III}-2LI) by both vapor diffusion of diethyl ether into a dimethylformamide (DMF) solution of the complex (Type A), and by recrystallization from hot DMF (Type B) (Figure 2 and Figure S1 in Supporting Information). The crystals were found to have either one or two crystallographically independent complex molecules, depending on the crystallization technique. The crystallographic data is given in Table S1 and selected bond lengths are given in Table 1. In the absence of Tb^{III} and Dy^{III} structures of the Ln^{III}-5LIO com-

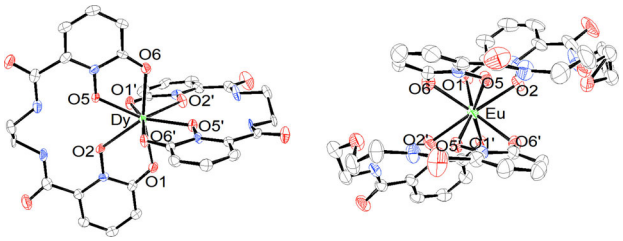

Figure 2. ORTEP diagrams of $[Dy^{III}(2LI\text{-}1,2\text{-}HOPO)_2]PyH$ (this work) and $[Eu^{III}(5LIO\text{-}1,2\text{-}HOPO)_2]PyH$.[11a] Counterions, solvent molecules and hydrogen atoms have been omitted for clarity; displacement ellipsoids drawn at 50% probability.

plex, and in order to illustrate the expected structure of these complexes, an ORTEP diagram of a Eu^{III}-5LIO[11a] structure is also presented in Figure 2. The coordinates of this structure and a Gd^{III}-5LIO structure[11b] are used in the ab initio calculations discussed below. The coordination sphere of the complexes is comprised of four negatively charged pyridinolate and four keto oxygens. In the crystal structures presented here, two different arrangements of these donors around the metal center are observed, as illustrated in Figure 3, which represents that of the *a*-edged Ln^{III}-2LI structure, in which the O_{pyO} donors occupy the axial positions (with an angle of $\approx 60^\circ$ between them), while the O_{ket} are arranged in the equatorial position. Figure 3c illustrates the *g*-edged *trans* structure of Eu^{III}-5LIO and Gd^{III}-5LIO, where the different donors are distributed alternately, and this is expected to be the case for the Dy^{III}-5LIO and Tb^{III}-5LIO structures. The *g*-edged *cis* mode in which the donors are also distributed alternately (Figure 3b) has been observed in a Sm^{III}-5LIO crystal structure.[9,11]

Comparison of the bond lengths indicates no significant difference between the two types of donors. In the case of the *a*-edged structures the Ln–O_{pyO} and Ln–O_{ket} bond lengths differ by only 0.019–0.043 Å, whereas the bond lengths of the Gd^{III} *g*-edged structure exhibit the opposite trend. The Eu^{III} structure does not exhibit any strong trend between donor type and bond length. It may be concluded that the coordination bond lengths are more strongly influenced by steric effects of the ligand rather than electronic properties of the donor atoms. Continuous shape analysis of each structure was carried out using the program SHAPE 2.1,[12] and the continuous shape measures (CShM) are also presented in Table 1. The CShM is a dimensionless value which ranges from 0 to 100, 0 indicating the perfect polyhedron.[13] According to these values, the coordination spheres of the Ln^{III}-2LI structures are closest to a triangular dodecahedron (TDD, D_{2d}) and bisaugmented trigonal prism (BTPR, C_{2v}), whereas the Ln^{III}-5LIO structures exhibit geometries closest to a regular square anti-prism (SAPR, D_{4d}). From these results the Ln^{III}-2LI geometry would be expected to promote a larger magnetic anisotropy for both Tb^{III} and Dy^{III} than the Ln^{III}-5LIO geometry.[14] This conclusion is however misleading, and when comparing the CShM values between the different complexes for these three ideal geometries, the values of the Ln^{III}-5LIO complexes are consistently smaller than the Ln^{III}-2LI structures. For SAPR, TDD, and BTPR, the average CShM values of Ln^{III}-5LIO are 1.4, 2.1, and 2.5, respectively. For the

Table 1. Selected bond lengths [Å] of crystal structures utilized in the ab initio calculations (see below) and SHAPE analysis of crystal structures. Note numbering of the oxygen atoms is only valid for the structures published here.

	a-edged						*g*-edged	
	Tb^{III}-2LI (Type A)	Tb^{III}-2LI[a] (Type A)	Tb^{III}-2LI (Type B)	Dy^{III}-2LI (Type A)	Dy^{III}-2LI[a] (Type A)	Dy^{III}-2LI (Type B)	Eu^{III}-5LIO[b]	Gd^{III}-5LIO[c]
Dy–O^{2}_{pyO}	2.339(3)	2.335(3)	2.358(2)	2.350(3)	2.337(3)	2.334(7)	2.372(3)	2.331(10)
Dy–O^{5}_{pyO}	2.357(2)	2.364(2)	2.402(2)	2.326(3)	2.328(3)	2.356(5)	2.434(3)	2.325(10)
Dy–$O^{2'}_{pyO}$	2.366(2)	2.335(2)	2.346(2)	2.319(4)	2.356(3)	2.359(7)	2.371(3)	2.328(10)
Dy–$O^{5'}_{pyO}$	2.332(3)	2.347(2)	2.334(2)	2.358(3)	2.328(3)	2.336(6)	2.457(3)	2.344(9)
Dy–O^{1}_{ket}	2.388(3)	2.402(3)	2.388(2)	2.357(3)	2.375(3)	2.374(6)	2.383(3)	2.295(8)
Dy–O^{6}_{ket}	2.365(2)	2.370(3)	2.376(2)	2.382(3)	2.391(3)	2.368(7)	2.380(3)	2.323(12)
Dy–$O^{1'}_{ket}$	2.375(2)	2.400(3)	2.407(2)	2.389(3)	2.362(3)	2.393(5)	2.394(3)	2.331(10)
Dy–$O^{6'}_{ket}$	2.399(2)	2.383(3)	2.381(2)	2.365(3)	2.388(3)	2.328(6)	2.385(3)	2.265(10)
Dy–O^{av}_{pyO}	2.349	2.345	2.360	2.338	2.337	2.347	2.409	2.332
Dy–O^{av}_{ket}	2.382	2.367	2.388	2.373	2.379	2.362	2.386	2.304
Dy-O^{av}_{ket}–Dy-O^{av}_{pyO}	0.033	0.022	0.028	0.035	0.042	0.015	-0.023	-0.028
Square anti-prism (SAPR, D_{4d})	5.231	5.661	6.482	5.068	5.448	5.311	1.397	1.422
Triangular dodecahedron (TDD, D_{2d})	3.884	4.223	4.205	3.679	4.073	3.332	2.233	2.044
J-Bisaugmented trigonal prism[d] (JBTPR, C_{2v})	4.158	4.221	4.967	4.043	4.081	4.461	3.358	2.930
Bisaugmented trigonal prism[d] (BTPR, C_{2v})	3.482	3.432	4.298	3.367	3.277	3.686	2.628	2.419
J-snub disphenoid[d] (JSD, D_{2d})	4.690	5.059	4.840	4.559	4.939	4.173	5.504	5.342

[a] Two independent complex molecules are present in the asymmetric unit of the Type A crystal structures. In the CIF the labels of this molecule appear with an "a" in the notation to distinguish it from the other molecule, for example, O1′ appears as O1a". [b] Previously published structure from ref. [11a]. [c] Previously published structure from ref. [11b]. [d] J indicates a Johnson polyhedron, that is, having regular faces and all edges the same length, the BTPR on the other hand is spherical with nonequivalent edges.

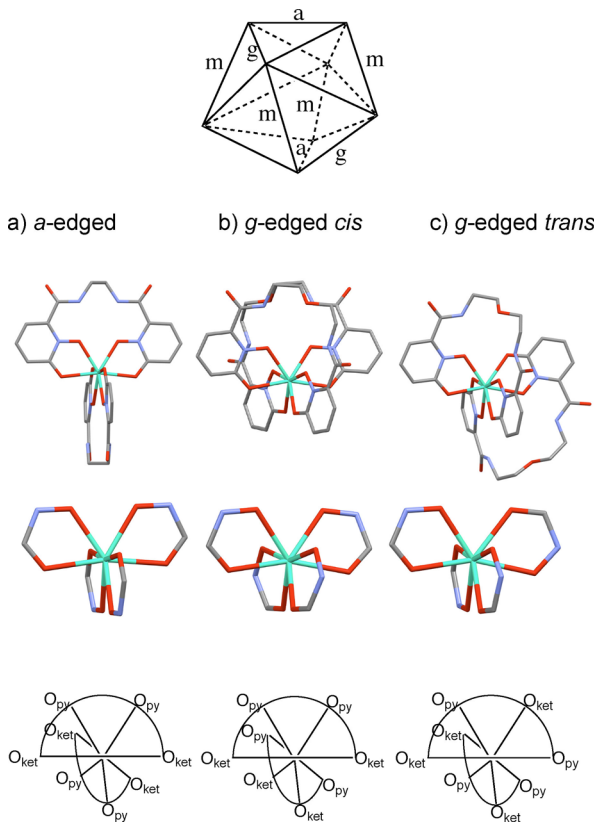

Figure 3. The dodecahedron has been reproduced from ref. [10] and illustrates the *a*- and *g*-edges occupied by the ligand backbones, *m*-edges are always occupied by the bidentate 1,2-HOPO moieties. Optimized structures and illustration of donor distribution for (a) *a*-edged (Ln^{III}2LI), (b) *g*-edged *cis*, and (c) *g*-edged *trans* (Ln^{III}5LIO) coordination modes.

Ln^{III}-2LI structures, these values range 6.5–5.1, 4.2–3.3, and 4.3–3.3, respectively. It is also important to reiterate that these values can range from 0–100. An overlay of the ideal geometries with the first coordination sphere of the Gd^{III}-5LIO and Tb^{III}-2LI (type B) is given in Figure S2 and illustrates more clearly the differences indicated by the CShM values. Close inspection of the Ln^{III}-5LIO structure reveals axial elongation of the SAPR, which is expected to increase the anisotropy of both Tb^{III} and Dy^{III}.[14] Additionally, the distribution of different bond lengths will have an effect on the overall anisotropy of each complex, making a simple comparison with ideal geometries slightly challenging. As stated above, in the Ln^{III}-2LI complexes, the axial Ln–O_{py} bond lengths are slightly shorter than those in the equatorial region, which may assist in promoting a larger anisotropy of both complexes.[15]

DFT optimized structures

In order to represent the solution-state structures present in the MCD, DFT geometry optimizations of the Dy^{III} complexes were performed (B3LYP/6-31G(d,p) for C, H, N, and O; MWB55[16] for Dy^{III}). Previously published Eu^{III} optimized structures were used as input structures.[9a] Plots of the final structures are presented in Figure S8 and the output coordinates are also provided as Supporting Information. Only the lowest energy conformations were considered, as these are expected to be the predominant species in solution, that is, *a*-edged for Dy^{III}-2LI, and *g*-edged for Dy^{III}-5LIO (see Table S5).[9a] As expected, the optimized structures show higher symmetry than the crystal structures, with two sets of equivalent bond lengths for the *a*-edged complexes and four sets of equivalent bond

lengths for the *g*-edged complexes (Table S6). As observed in the crystal structures of the *a*-edged species the Dy–O_{pyO} bonds are slightly shorter than the Dy–O_{ket} distances. For the *g*-edged species, however, the opposite is observed for the *cis* configuration, while no significant difference is observed for the *trans* structure. Continuous shape analysis was also performed on the optimized structures; the results can be found in Table S6.

Electronic properties

i. Magnetism

Magnetic susceptibilities of the Ln^{III}-2LI and Ln^{III}-5LIO complexes were measured on powder samples at 0.05 and 0.1 Tesla over the temperature range 2–300 K. The $\chi_M T$ versus T plots are presented in Figure 4 i. The room temperature values amount to 12.27(11), 10.52(9), 14.81(13), and 13.92(13) $cm^3 K mol^{-1}$, for compounds Tb^{III}-2LI, Tb^{III}-5LIO, Dy^{III}-2LI, and Dy^{III}-5LIO, respectively. The values of the Ln^{III}-5LIO complexes are below the respective free ion values, whereas the Ln^{III}-2LI complexes are slightly above these values (Tb^{III} = 11.82, Dy^{III} = 14.17 $cm^3 K mol^{-1}$). The values are, however, within the range previously found for mononuclear Dy^{III} and Tb^{III} complexes.[17] The magnetic susceptibilities experience a slight decrease with decreasing temperature which we attribute to depopulation of the ground state M_J levels ($^7F_6$ and $^6H_{15/2}$ for Tb^{III} and Dy^{III}, respectively). The more pronounced drop at low temperature is likely due to magnetic anisotropy. Low temperature field dependent magnetization was measured for all complexes. Experimental values were found the be significantly lower than the theoretical values for $M_J = \pm 6$ and $M_J = \pm 15/2$ ground states (9 and 10 μ_B, respectively), and non-saturation of magnetization at high field suggests the presence of appreciable magnetic anisotropy and/or of low-lying excited states (Figure 4 ii).[18] This conclusion is supported by non-superposition of the M vs. B/T plots at higher field (see Figure S3).[19]

ii. High-frequency electron paramagnetic resonance (HF-EPR)

Fixed powder HF-EPR spectra were collected for both Ln^{III}-2LI and Ln^{III}-5LIO complexes of Tb^{III} and Dy^{III}, however, the Dy^{III} spectra show a broad resonance feature with a wide line width of 3 T, which is not clear enough to be evaluated. In the HF-EPR spectra of the Tb^{III}-2LI and Tb^{III}-5LIO complexes, one single resonance feature is observed in the magnetic field range of 0 to 16 T. A selection of the low temperature spectra of both Tb^{III} complexes is presented in Figure 5, with resonance fields measured at various frequencies. In the frequency range studied, the single resonance feature appears at low magnetic fields ($B < 2$ T) and no additional resonance features are observed at higher temperatures (see Figure S4 in Supporting Information). The resonance fields displayed in Figure 5 show linear dependence on frequency, with a slope much steeper than the *g*-factor $g = 1.5$ of the allowed transition. We hence attribute the resonances to forbidden transitions. By a linear fitting of the data, the *g*-value and the zero field splitting (ZFS) are estimat-

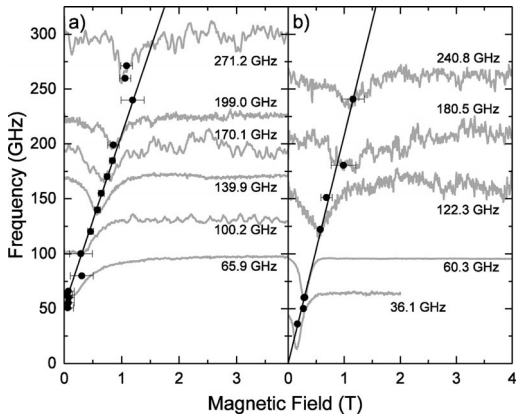

Figure 5. Resonance field position of (a) Tb^{III}-2LI and (b) Tb^{III}-5LIO complexes at various frequencies, at 2 K. Representative EPR spectra are shown with corresponding frequency values. The solid lines represent the linear fitting lines. See the text for the fitting parameters.

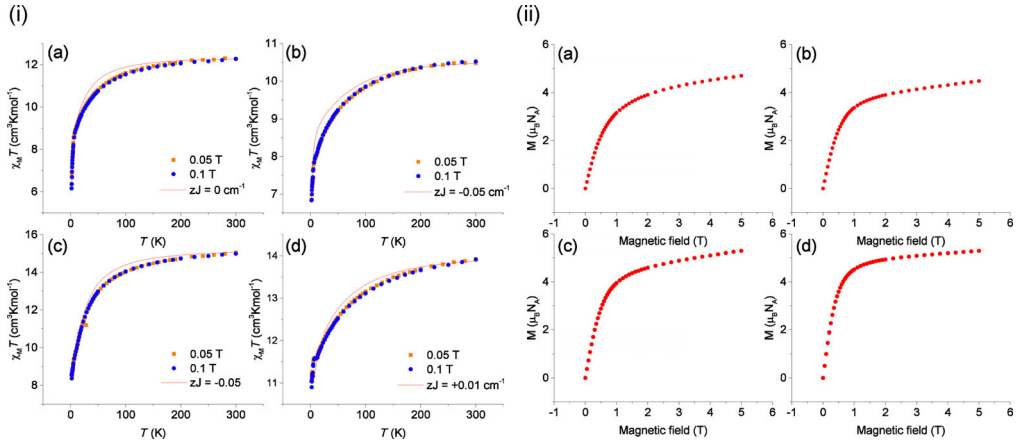

Figure 4. Magnetic susceptibility times T (i) and static field magnetization ($T = 2$ K) (ii) of (a) Tb^{III}-2LI, (b) Tb^{III}-5LIO, (c) Dy^{III}-2LI, and (d) Dy^{III}-5LIO (the full lines in the magnetic susceptibility curves are simulations based on the ab initio calculations, see below).

ed to be $g=11(2)$ and $\Delta_{ZFS}=52(4)$ GHz for Tb^{III}-2LI, and $g=15(8)$ for Tb^{III}-5LIO. Δ_{ZFS} of Tb^{III}-5LIO is negligible. For the Tb^{III}-2LI complex, no EPR signal is observed below 44 GHz down to the lowest frequency of our experimental set-up.

The observed single resonance feature in a wide magnetic field and temperature range indicates that the resonance originates from the ground state excitation, with a reasonably large energy difference between the ground state and the first excited state, that is, $\Delta \geq 20$ K (14 cm^{-1}). In the general case of a system with no single ion anisotropy resulting in no ZFS, all of the resonances overlay in the same magnetic field and it appears as only a single resonance feature in the EPR spectra with $g_{Landé}$. However, the anisotropy of Tb^{III} is not negligible and is supposed to cause state mixing. Correspondingly, the observed resonance shows a large g-value implying that the resonance is due to a forbidden transition that does not follow the conventional magnetic dipole selection rule. Due to the large energy difference between the ground state and the excited state, conventional (so-called allowed) resonances following the selection rule do not show up in the studied frequency range, but only the forbidden resonance appears, which is observed in the specific magnetic field orientation where state mixing is induced by transverse anisotropy. This is corroborated by the experimental data, since the observed resonance does not exhibit the typical shape for a powder EPR spectrum. Applying the Landé g-factor of the Tb^{III} ion, $g_{Landé}=1.5$, the slopes of the resonance branches suggest differences of the angular momentum, corresponding to the energy states related to the resonance of about 7.4 and 10 for Tb^{III}-2LI and Tb^{III}-5LIO, respectively. In the case of an integer angular momentum like Tb^{III} ($J=6$), the possible transition with the above g-factors is $M_J=-4\rightarrow+4$ and $M_J=-5\rightarrow+5$ for Tb^{III}-2LI and Tb^{III}-5LIO, respectively. Hence, the HF-EPR data suggest for both complexes that the $M_J=6$ state is not the ground state, leading to the conclusion that the studied complexes lack axial symmetry. It is interesting that a ZFS is observed for the Tb^{III}-2LI complex, whereas not for the Tb^{III}-5LIO complex. The observed ZFS in the Tb^{III}-2LI complex may be ascribed to the energy splitting between the ground doublet states, which is induced by the transverse anisotropy. The absence of a ZFS in Tb^{III}-5LIO can hence be understood in terms of a relatively weak transverse anisotropy that might be so small that the ZFS is not resolved, and this conclusion is consistent with the ab initio results (see Table 5 below). However, due to the non-negligible transverse anisotropy and misalignment of spins in the fixed powder sample, the forbidden resonance still appears.

iii. Magnetic circular dichroism spectroscopy (MCD)

In order to illustrate the subtle ligand field effects of the two main binding modes on the M_J splitting, MCD spectra of the Dy^{III} complexes were measured. The transitions of Tb^{III} occur largely outside the measurable range of our experimental set-up and these complexes were not measured. Spectra of the Dy^{III} complexes were obtained from glass samples in 1:2 MeOH/DMF solutions at 5 T over the temperature range 2–75 K. An overview of the full spectra of both complexes can be found in Figures S5–S6 of the Supporting Information, with assignments of the bands to the appropriate multiplets. Detailed spectra of selected transitions are shown in Figure 6. The absorption electronic spectra were also measured, but were of low quality due to small extinction coefficients and large background noise. The very weak ΔA signals are easily detected with the phase-sensitive detection used in MCD, and the f–f-transitions are distinctly observed. Dy^{III} has 1001 Kramers doublets, of which 46 are expected to occur within the range of 9000–23000 cm^{-1}. These correspond to the multiplets $^6H_{9/2}$, $^6H_{7/2}$, $^6H_{5/2}$, $^6F_{11/2}$, $^6F_{9/2}$, $^6F_{7/2}$, $^6F_{5/2}$, $^6F_{3/2}$, $^6F_{1/2}$, $^4F_{9/2}$ and $^4I_{15/2}$. The transition $^6H_{15/2}\rightarrow{}^6F_{1/2}$ is forbidden due to $\Delta J>6$, and is not observed experimentally.[20] The energies of these transitions are predominantly determined by the free ion terms and the spectra appear to be very similar. However, small features, such as hot bands, differences in relative intensities, and slight

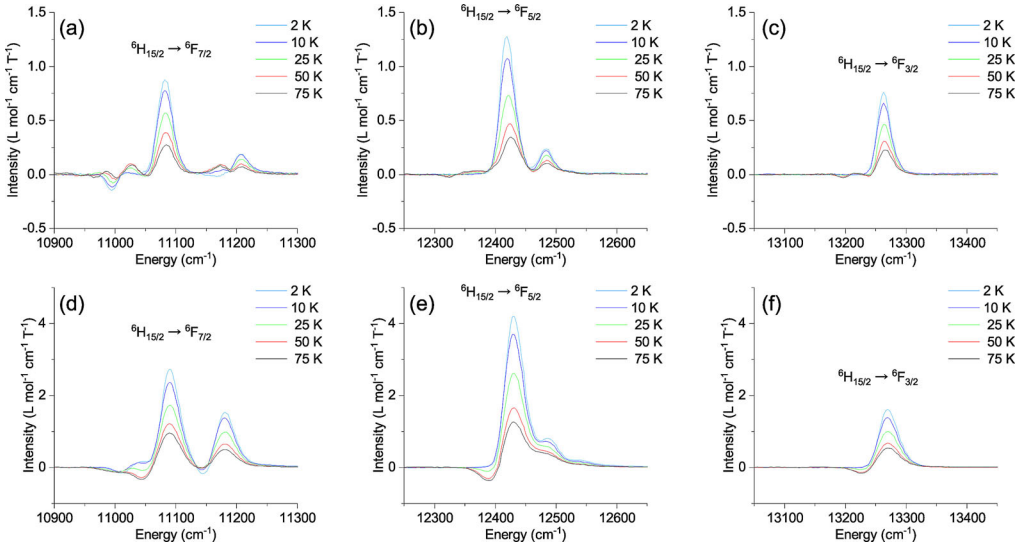

Figure 6. Temperature dependence of selected MCD transitions of Dy^{III}-2LI (a–c) and Dy^{III}-5LIO (b–f).

shifts in energy reveal differences in the ligand field splitting of the multiplet levels. The individual transitions were carefully extracted using the fitting function in OriginPro 2017.[21] Spectra at all measured temperatures were analyzed in order to obtain a consistent set of energies and relative intensities of both the main transitions and hot bands.

Details of all the fitted transitions, along with illustrations of the fits of the 2 and 75 K spectra are provided in Tables S2–3 and Figure S7. In some cases the number of fitted transitions does not correspond to the number of transitions theoretically expected. As the spectra were measured in frozen solution and the complexes lack perfect symmetry, the usual selection rules do not apply and it was considered more accurate to fit the spectra without adhering to strict theoretical constraints. Coincidence of the energies of the $^6H_{9/2}$, $^6H_{7/2}$ multiplets with the $^6F_{11/2}$, $^6F_{9/2}$ multiplets, respectively, results in a large number of transitions in both these regions; nonetheless, a best attempt to extract these transitions was made and can be found in the Figure S7. The transition $^6H_{15/2} \rightarrow {}^6H_{5/2}$ is observed around 10250 cm^{-1} but was considered too weak to fit. Figure 6 presents the temperature dependence of the transitions $^6H_{15/2} \rightarrow {}^6F_{7/2}$, $^6F_{5/2}$, and $^6F_{3/2}$, for both Dy^{III}-2LI and Dy^{III}-5LIO. These transitions show clear C-term behavior, as is expected for a system possessing a degenerate ground state. Decreasing signal intensities with increasing temperature indicate that the population of the upper level of the split Kramers doublet is of the opposite sign, leading to cancellation of the low temperature transitions, and means the energies of the transitions originating from the two components of the split doublet are not resolved. Hot bands can be observed with increasing temperature and are due to transitions from thermally occupied low-lying excited states. The respective energy shifts of the hot bands for the transitions to multiplets $^6F_{5/2}$ and $^6F_{3/2}$ were found to be about 100 and 70 cm^{-1} for Dy^{III}-2LI, and 40 cm^{-1} for both transitions of Dy^{III}-5LIO. These negative signals appearing at lower energy to the main peaks indicate that the effective *g*-value in this thermally populated state is of the opposite sign to the ground state. The larger intensities of these signals of Dy^{III}-5LIO in comparison to Dy^{III}-2LI are indicative of a greater effective *g*-value of the ground state of Dy^{III}-5LIO. It is difficult to compare this with the calculations (Table 2), as it depends on the polarization of the intensities as to which direction of the magnetic field is most effective at induced MCD intensity. In low-temperature glass where the molecules are randomly oriented, it would appear that MCD for light parallel to g_z is more effective at including MCD intensity in the Dy^{III}-5LIO complex as compared to the Dy^{III}-2LI complex.

iv. Ligand field calculations

The results of a full f^9 ligand field calculation are shown in Figure 7 as a stick spectrum, indicating the upper state multiplet of the various transitions, and these calculated energies as well as the experimental energies are presented in Table S4. The Hamiltonian has been described previously,[7b] and includes electron repulsion (F^k), spin-orbit coupling (ζ), two body configuration interaction terms (α, β, γ), the three body parameters (T^k), the magnetic parameters (M^k) describing spin-spin and spin-other orbit interaction, and the electrostatically correlated spin-orbit interaction (P^k). The ligand environment is accounted for by using the Angular Overlap Model (AOM), which uses structural information about the complex and parameters that describe the weak σ and π bonding interactions. The calculation has been made in the full 2002×2002 basis of all f^9 free ion states, with symmetry used where possible to block the matrices.

The 2LI ligand in either D_2 or S_4 symmetry (see Figure 8) is attractive as it can be determined with a small number of parameters. The 8 coordinating oxygen atoms have two unique positions, which are related to the others by the C_2 or S_4 axes. This means that there are only two sets of AOM angles, θ, ϕ, and two sets of bonding parameters, e_σ, e_π. However, it is expected that the π-bonding will be anisotropic due to the five membered chelating ring with aromatic character. We define the χ angle in Table 3 such that the local ligand *y*-axis is directed within the plane containing the Dy^{III} and the two oxygens of the ring (see Figure 8). There are two e_π parameters with respect to these local axes and one would expect $e_{\pi x} > e_{\pi y}$. The definition of the AOM angles has been described in detail.[22] The description of the ligand field in terms of the AOM parameters is entirely equivalent to the use of the crystal field parameters as given in ref. [23]. The 27 possible B_{kq}, B_{kq}' parameters are related to the 27 matrix elements of 7×7 AOM matrix in the basis of real f orbitals (upper triangle-trace) as given in the literature.[24]

For anisotropic π-bonding, one requires the AOM factors using all three angles, and this may be achieved by substituting the Eulerian transformation matrix for the directional cosines in Equation (5) and Table 1 of Urland,[24] resulting in the $F^{(f)}$ matrix. While the AOM is equivalent to the CF parameteriza-

Table 2. Ab initio calculated first excitation energies and total coefficients of the M_J projections of the RASSI coupled wave function of the Kramers doublets (KD) of the optimized structures. Details of all the $^6H_{15/2}$ doublet levels are given in Tables S9–S10.

	KD 1		KD 2	
	Energy [cm^{-1}]	Coefficients	Energy [cm^{-1}]	Coefficients
Dy^{III}-2LI-*a*-D_2	0	0.75 | ±15/2>; 0.18 | ±7/2>	48.55	0.26 | ±5/2>; 0.22 | ±3/2>; 0.14 | ±9/2>; 0.13 | ±7/2>; 0.11 | ±11/2>; 0.10 | ±1/2>
Dy^{III}-2LI-*a*-S_4	0	0.77 | ±15/2>; 0.19 | ±7/2>	56.301	0.52 | ±5/2>; 0.29 | ±3/2>; 0.10 | ±11/2>
Dy^{III}-5LIO-*g-trans*	0	0.41 | ±9/2>; 0.30 | ±13/2>; 0.12 | ±15/2>	10.543	0.60 | ±11/2>; 0.12 | ±9/2>; 0.10 | ±7/2>
Dy^{III}-5LIO-*g-cis*	0	0.76 | ±15/2>; 0.12 | ±11/2>	12.433	0.44 | ±1/2>; 0.29 | ±3/2>; 0.11 | ±5/2>

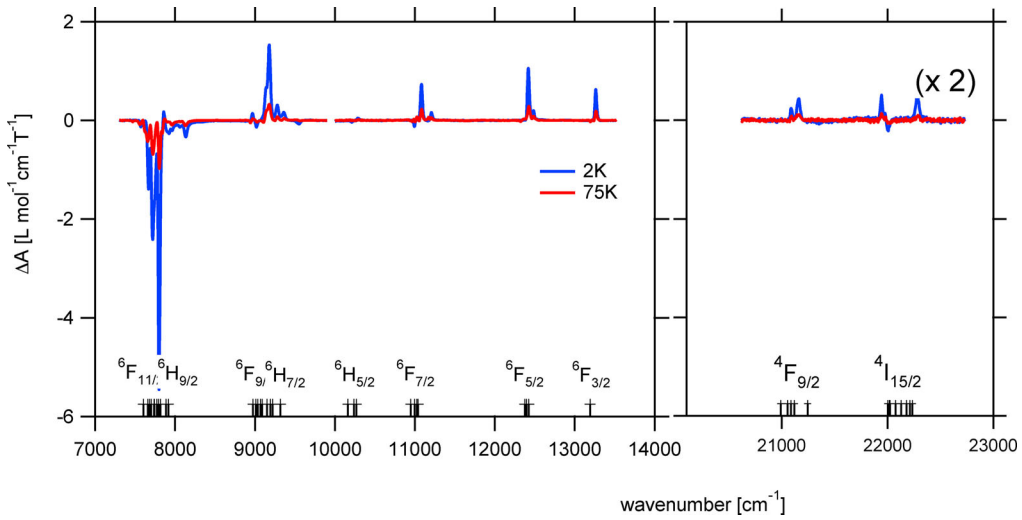

Figure 7. The MCD spectra of Dy^{III}-2LI at 5 Tesla and 2 K (blue) and 75 K (red). The calculated energies are shown as stick plots below with the excited state multiplet involved in the transition. The calculated energies are using the geometry and parameters of Tables 3 and 4, together with the free ion values from ref. [27].

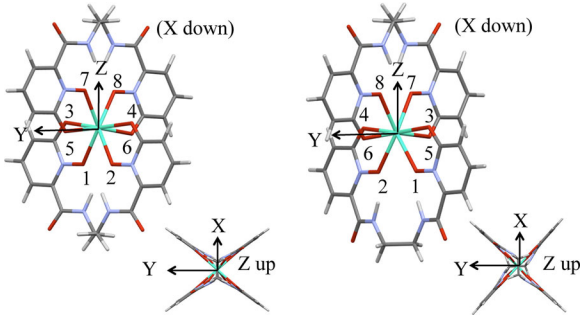

Figure 8. Orientation of *xyz*-axes for definition of AOM angles of Dy^{III}-2LI-*a*-D_2 (left) and Dy^{III}-2LI-*a*-S_4 (right).

tion, it remains to be seen how chemically meaningful the parameters are. They are not well defined, but the trend from previous studies is that $e_\sigma < 400\ cm^{-1}$ is smaller and the $e_\pi/\ e_\sigma$ ratio is larger than in transition metal complexes. The e_π anisotropy has previously been shown to be significant in a polarized spectral study.[25] A drawback of using crystal field parameters is that the same ligand field can be described by a completely different set of parameter values depending on the definition of the coordinate system. This is a particular problem with low symmetry complexes, and is important because the choice of coordinate system defines the basis functions and the description of the electronic state. For example, if one is seeking a ground state with a high $|\pm M_J>$ value, this will depend on the definition of the coordinate system.

The ligand field parameters of the Dy^{III} complexes have also been calculated with an established ab initio approach, as coefficients to extended Stevens operators (ESO) as zero field parameters in a pseudo spin Hamiltonian, with an effective $S = 15/2$ ground state (see below), and are presented in Table S7 of the Supporting Information.[26] Much similar information can

Table 3. Defined AOM angles for Dy^{III}-2LI-*a*-D_2 and Dy^{III}-2LI-*a*-S_4.

	L	e_σ	$e_{\pi x}$	$e_{\pi y}$	θ	ϕ	χ	
D_2	O1	$e_{\sigma 1}$	$e_{\pi x 1}$	$e_{\pi y 1}$	$180-\theta_1$	ϕ_1	$90-\chi_1$	$\theta_1 = 33.05$, $\phi_1 = 38.12$, $\chi_1 = 11.83$
	O2	$e_{\sigma 1}$	$e_{\pi x 1}$	$e_{\pi y 1}$	$180-\theta_1$	$180+\phi_1$	$90-\chi_1$	$\theta_2 = 83.69$, $\phi_2 = 48.80$, $\chi_2 = 6.46$
	O3	$e_{\sigma 2}$	$e_{\pi x 2}$	$e_{\pi y 2}$	θ_2	ϕ_2	$90-\chi_2$	
	O4	$e_{\sigma 2}$	$e_{\pi x 2}$	$e_{\pi y 2}$	θ_2	$180+\phi_2$	$90-\chi_2$	
	O5	$e_{\sigma 2}$	$e_{\pi x 2}$	$e_{\pi y 2}$	$180-\theta_2$	$180-\phi_2$	$90-\chi_2$	
	O6	$e_{\sigma 2}$	$e_{\pi x 2}$	$e_{\pi y 2}$	$180-\theta_2$	$-\phi_2$	$90-\chi_2$	
	O7	$e_{\sigma 1}$	$e_{\pi x 1}$	$e_{\pi y 1}$	θ_1	$180-\phi_1$	$90-\chi_1$	
	O8	$e_{\sigma 1}$	$e_{\pi x 1}$	$e_{\pi y 1}$	θ_1	$-\phi_1$	$90-\chi_1$	
S_4	O1	$e_{\sigma 1}$	$e_{\pi x 1}$	$e_{\pi y 1}$	$180-\theta_1$	$270-\phi_1$	$90-\chi_1$	$\theta_1 = 32.41$, $\phi_1 = 39.53$, $\chi_1 = 5.96$
	O2	$e_{\sigma 1}$	$e_{\pi x 1}$	$e_{\pi y 1}$	$180-\theta_1$	$90-\phi_1$	$90-\chi_1$	$\theta_2 = 83.93$, $\phi_2 = 45.09$, $\chi_2 = 3.21$
	O3	$e_{\sigma 2}$	$e_{\pi x 2}$	$e_{\pi y 2}$	θ_2	$180+\phi_2$	$90-\chi_2$	$r_1 = 2.382$ Å (Dy–O1, O2, O7, O8)
	O4	$e_{\sigma 2}$	$e_{\pi x 2}$	$e_{\pi y 2}$	θ_2	ϕ_2	$90-\chi_2$	$r_2 = 2.428$ Å (Dy–O3, O4, O5, O6)
	O5	$e_{\sigma 2}$	$e_{\pi x 2}$	$e_{\pi y 2}$	$180-\theta_2$	$270+\phi_2$	$90-\chi_2$	
	O6	$e_{\sigma 2}$	$e_{\pi x 2}$	$e_{\pi y 2}$	$180-\theta_2$	$90+\phi_2$	$90-\chi_2$	
	O7	$e_{\sigma 1}$	$e_{\pi x 1}$	$e_{\pi y 1}$	θ_1	$-\phi_1$	$90-\chi_1$	
	O8	$e_{\sigma 1}$	$e_{\pi x 1}$	$e_{\pi y 1}$	θ_1	$180-\phi_1$	$90-\chi_1$	

be gained about the magnetic properties of the ground state as in a full ligand field calculation, but it remains to be seen whether the two approaches are consistent. It therefore is of interest to compare the ab initio calculated values with ligand field parameters obtained in a full f^9 diagonalization. Ryabov has given relationships between the standard Wybourne B_{kq} parameters and the B_{kq}(ESO) parameters, by considering the B_{kq} operating within a particular LSJ multiplet.[28] However, the multiplet that the ligand field operates in is only 93% pure $^6H_{15/2}$ multiplet; spin-orbit coupling and other atomic terms mix other $J=15/2$ free ion states such as $^4I(3)_{15/2}$ and $^4I(1)_{15/2}$. Ideally, one should diagonalize the atomic terms and take the eigenvectors of the lowest multiplet as a basis for further calculation with the ligand field. Then a direct comparison could be made with the ligand field matrix elements within the lowest multiplet and those of the ESO basis. However, this proved difficult as the degenerate set of 16 eigenvectors found with such an approach has to be ordered appropriately according to M_J values and, importantly, the phases need be fixed to allow a comparison of matrix elements.

A much easier approach is to calculate B_{kq} from B_{kq}(ESO) and then fit the AOM parameters to these B_{kq} values by varying the e_σ, e_π parameters. For the Dy^{III}-2LI complex, the B_{kq}(ESO) have been calculated for both D_2 and S_4 symmetry (Tables S7–S8). These symmetries will have 9 and 7 B_{kq} parameters when the coordinate system is aligned with the symmetry axes. In D_2 all imaginary terms are zero, with the non-zero terms listed in Table 4.

Table 4. Ab initio calculated and fitted ligand field parameters and the corresponding fitted AOM parameters for Dy^{III}-2LI-*a*-D_2.

k	*q*	B_{kq} (CASSCF) [cm^{-1}]	B_{kq} (AOM Fit) [cm^{-1}]	AOM parameters
2	0	138.889	137.203	$e_{\sigma1}=236.2$
2	2	−53.727	−12.241	$e_{\pi x1}=112.8$
4	0	96.663	98.589	$e_{\pi y1}=49.0$
4	2	201.820	194.920	$e_{\sigma2}=223.9$
4	4	−639.759	−643.757	$e_{\pi x2}=49.1$
6	0	−756.937	−756.740	$e_{\pi y2}=66.6$
6	2	12.153	11.145	
6	4	251.911	249.755	
6	6	196.626	196.723	

The B_{kq}(ESO) parameters, with the extended Stevens operators in the $S=15/2$ basis, give exactly the same eigenvalues if the equivalent B_{kq} parameters are used in a $^6H_{15/2}$ multiplet in isolation (as mentioned above, this is not strictly true). The pseudo spin approach can also include higher order zero field terms for $k=8,10,12$, but these terms are small and their neglect changes the eigenvalues by $<1\ cm^{-1}$. A similar approach was made for the S_4 geometry but in this case there were some non-negligible B_{kq}(ESO) components inconsistent with S_4 symmetry (B_{22}, B_{42}, B_{62}, B_{66}). If these were ignored, the AOM fit could not be consistently made.

The AOM values listed in Table 4 are not unreasonable values. For each independent ligand set $e_\sigma > e_\pi$. The AOM parameters $e_{\sigma1} > e_{\sigma2}$ are consistent with $r_1 < r_2$, that is, the axial ligands having slightly shorter bond lengths. The out-of-plane π-bonding is larger than the in-plane for the axial ligands ($e_{\pi x1} > e_{\pi y1}$), as expected; but not for the equatorial ligands. Therefore, the pseudo spin Hamiltonian used appears to give chemically reasonable parameters, making it a promising approach to determine a large number of parameters in low symmetry lanthanide complexes.

v. Quantum chemical ab initio calculations of the electronic properties

In order to evaluate the experimental data and compare the various experimental approaches and the ligand field calculations, the electronic and magnetic properties and ligand field parameters were also calculated with a well-established quantum chemical approach. Wave functions were computed ab initio with MOLCAS 8.0. Calculations were carried out on the crystal structure coordinates of Dy^{III}-2LI, Tb^{III}-2LI (this work), Eu^{III}-5LIO and Gd^{III}-5LIO.[11] All counter ions, solvent molecules and (if present) disorder in the crystal structures have been omitted from the input structural data. For the purpose of analysis of the MCD results, calculations were also carried out on DFT optimized Dy^{III} structures (see Experimental Section). ANO-RCC-TZVP basis sets were used to describe all atoms except hydrogen (DZV). Active spaces of eight and nine electrons (for Tb^{III} and Dy^{III}, respectively) in seven 4f orbitals were selected for the complete active space self-consistent field method (CASSCF).[29] The inclusion of dynamic correlation (second-order perturbation theory) was not considered necessary, as it is known to have only small effects for lanthanides.[30] For Tb^{III} ($4f^8$), there exist 7 septet, 140 quintet, 200 triplet, and 200 singlet states. In a balance of cost and accuracy, 7, 100, 100, and 100 states, were considered, respectively. For Dy^{III} ($4f^9$) of the 21 sextet, 224 quartet, and 490 doublet states, all sextet, 100 quartet, and 100 doublet states were considered.[7b] Spin-orbit coupling was introduced to the spin-free wave functions in each case through the restricted active space state interaction method (RASSI).[5a] Due to the large number of states and associated calculation cost, only a limited number of states can be mixed by spin-orbit coupling. Therefore, for Tb^{III} all septet, 50 quintet, triplet, and singlet states were included. Similarly, all sextet, 50 quartet and doublet states were included for Dy^{III}. Finally, the MOLCAS SINGLE_ANISO module was utilized to calculate the local electronic and magnetic properties of each complex. The resulting energies, *g*-tensors, relative orientations of local magnetic axes, and decomposition of the RASSI wave functions are given in Table 5. Plots of the most likely relaxation pathways for complexes (c-3) and (d-1) are presented in Figure S10 and a summary for all Dy^{III} complexes is given in Table S11.

Simulations of the magnetic susceptibility of all measured complexes show acceptable agreement with the experimental data of the Ln^{III}-2LI and Ln^{III}-5LIO complexes (Figure 4i). Note that the simulation of Ln^{III}-5LIO was carried out using the Gd^{III}-

Table 5. Energies and properties of the first two pseudo-doublets and Kramers doublets of the Tb^{III} and Dy^{III} complexes (information of all doublets of the ground state multiplets are given in Tables S12–S15).

Doublets	Energy [cm^{-1}]	*g*-tensors g_x	g_y	g_z	D1-Dy-DX [°]	Total coefficients of the M_J projections of the RASSI coupled wave function
(a-1) Tb^{III}-2LI (Type A)						
1	0.000/ 8.133	0.000	0.000	14.6211	–	0.57 | ±6>; 0.21 | ±4>; 0.11 | ±2> / 0.68 | ±6>; 0.16 | ±4>
2	29.490/ 55.856	0.000	0.000	9.6272	22.3	0.37 | ±5>; 0.31 | ±3>; 0.20 | ±1> / 0.65 | ±5>; 0.16 | ±2>; 0.11 | ±3>
(a-2) Tb^{III}-2LI[a] (Type A)						
1	0.000/ 2.898	0.000	0.000	15.9450	–	0.73 | ±6>; 0.19 | ±4> / 0.79 | ±6>; 0.16 | ±4>
2	44.175/ 61.818	0.000	0.000	11.0712	24.1	0.49 | ±5>; 0.28 | ±3>; 0.14 | ±1> / 0.73 | ±5>; 0.18 | ±2>
(a-3) Tb^{III}-2LI (Type B)						
1	0.000/ 9.000	0.0000	0.0000	15.4563	–	0.65 | ±6>; 0.20 | ±4> / 0.78 | ±6>; 0.17 | ±4>
2	44.013	–	–	–	–	0.34 | ±3>; 0.29 | ±5>; 0.18 | ±1>; 0.16 | 0>
3	79.029/ 94.452	0.0000	0.0000	6.8173	82.5	0.38 | ±5>; 0.36 | ±3>; 0.12 | ±1> / 0.27 | ±1>; 0.25 | ±2>; 0.23 | 0>; 0.15 | ±6>
(b-1) Tb^{III}-5LIO[b]						
1	0.000/ 0.415	0.0000	0.0000	17.4955	–	0.94 | ±6> / 0.94 | ±6>
2	68.621/ 70.078	0.0000	0.0000	17.5321	89.3	0.61 | ±1>; 0.19 | ±3> / 0.44 | ±2>; 0.35 | 0>; 0.10 | ±1>
(b-2) Tb^{III}-5LIO[c]						
1	0.000/ 0.344	0.0000	0.0000	17.8574	–	0.99 | ±6> / 1.00 | ±6>
2	57.496/ 57.558	0.0000	0.0000	17.5679	84.7	0.78 | ±1>; 0.12 | ±3> / 0.48 | 0>; 0.39 | ±2>
(c-1) Dy^{III}-2LI (Type A)						
1	0	0.0494	0.9761	17.9039	–	0.80 | ±15/2>
2	80.544	0.6432	3.6560	13.0830	58.3	0.25 | ±9/2>; 0.17 | ±7/2>; 0.13 | ±11/2>; 0.12 | ±5/2>; 0.11 | ±13/2>; 0.11 | ±1/2>
(c-2) Dy^{III}-2LI[a] (Type A)						
1	0	0.0311	0.6303	18.1827	–	0.80 | ±15/2>
2	82.957	0.5768	1.0871	16.3512	45.5	0.24 | ±13/2>; 0.24 | ±9/2>; 0.20 | ±11/2>
(c-3) Dy^{III}-2LI (Type B)						
1	0.000	1.0006	1.6009	16.4739	–	0.74 | ±15/2>; 0.21 | ±7/2>
2	59.543	11.0495	7.5633	2.3655	3.14	0.51 | ±5/2>; 0.29 | ±3/2>
(d-1) Dy^{III}-5LIO[b]						
1	0	0.7791	2.8529	16.5771	–	0.71 | ±15/2>
2	17.822	0.9833	2.2310	15.6135	71.7	0.24 | ±1/2>; 0.21 | ±3/2>; 0.20 | ±5/2>; 0.13 | ±15/2>; 0.10 | ±7/2>
(d-2) Dy^{III}-5LIO[c]						
1	0	0.1101	0.4429	18.3100	–	0.81 | ±15/2>
2	36.549	0.0663	0.6558	17.3249	65.5	0.21 | ±5/2>; 0.20 | ±3/2>; 0.19 | ±7/2>; 0.16 | ±1/2>

[a] Two independent complex molecules are present in the asymmetric unit of the type A crystal structures. In the CIF the labels of this molecule appear with an "a" in the notation to distinguish it from the other molecule, for example, O1′ appears as O1a". [b] Calculations were carried out using the coordinates from the previously published Eu^{III}-5LIO crystal structure in ref. [11a]. [c] Calculations were carried out using the coordinates from the previously published Gd^{III}-5LIO crystal structure in ref. [11b].

5LIO crystal structure. The simulations using the Eu^{III}-5LIO structure coordinates are less satisfactory (Figure S11). This is likely due to the lanthanide contraction, the coordination bond lengths are expected to be such that $Eu^{III} > Gd^{III} > Tb^{III} > Dy^{III}$.[31] Therefore, it is reasonable to expect that the Gd^{III}-5LIO structure would more closely represent the structure of the Tb^{III} and Dy^{III} complexes. Additionally, the simulation of the Tb^{III}-5LIO magnetic susceptibility using the Eu^{III}-5LIO structure is notably better than that of the Dy^{III} analog, which may also be explained considering the relative ionic radii. This illustrates the high sensitivity of this computational method and the importance of using experimentally determined crystal structures.

The calculated *g*-tensors and composition of the ground state of the Tb^{III} complexes show acceptable qualitative agree-

ment with the HF-EPR results, and indicate that the *g*-edged binding mode induces a more axial ligand field/larger M_J ground state than the *a*-edged arrangement. From the calculations, the ground states of the two Dy^{III} complexes appear not to differ significantly. Due to inconclusive experimental data of the Dy^{III} complexes, however, no comparison can be made with these results.

Regarding the MCD results, the ab initio ligand field parameters as coefficients to the ESO of the optimized structures are presented in Table S7–S8; these have been converted to the standard Wybourne B_{kq} values given in Table 4 (see discussion above). The AOM parameters required to reproduce this ligand field can be found by varying e_σ, $e_{\pi x}$, $e_{\pi y}$ while keeping coordinates fixed (Table 3). The B_{kq} parameters found in this way, together with the "fitted" AOM parameters also given in Table 4, demonstrate that ab initio ligand field parameters are reasonable.

Considering now the potential SMM behavior of the four complexes, all first excitation energies are relatively small (Table 5), which increases the likelihood of thermally activated relaxation pathways. This is also illustrated in Figure S10. According to these results, quantum tunneling of magnetization is only relevant in the first excited state of Dy^{III}-2LI and Dy^{III}-5LIO (thermally activated quantum tunneling of magnetization, TA-QTM), despite mixing of the M_J states in both the ground and first excited states of all complexes, excluding the ground state of Tb^{III}-5LIO. This mixing induces significant transversal moments, and leads to reduced magnetic anisotropy. Note that the g_x and g_y values of Tb^{III} (non-Kramers ion) are zero according to Griffith's theorem.[32]

The orientations of the calculated magnetic axes of the two lowest states of structures (a-2), (b-2), (c-3) and (d-2) are illustrated in Figure 9, and the coordinates of the magnetic orientations of the remaining structures are given in Tables S16–S19 in Supporting Information. Non-alignment of the local magnetic axes is likely to promote Orbach and Raman relaxation processes.[33] In the case of the *a*-edged complexes, the axis of Tb^{III}-2LI is rotated approximately 34° in comparison to Dy^{III}-2LI, which is directed between the two sets of shorter Ln–O bonds of the pyridinolate oxygen donors. Due to relatively high symmetry of the type B Dy^{III}-2LI complex, the magnetic axis of the first excited state is well aligned with the ground state, however this is not the case for the type A structures (c-1) and (c-2), the first excited states of which are rotated by about 50°. The orientations of the two type A Tb^{III}-2LI structures are similar to each other, and the first excited state of both is rotated by about 20° from the ground state. The type B Tb^{III}-2LI shows different alignment of the ground state and rotation of about 80° of the third excited state (the second being a singlet state). The main magnetic axis of the ground state of the Tb^{III}-5LIO, calculated using the Gd^{III} structure (b-2), is oriented along C_4 axis of the twisted SAPR and rotates by 90° from the ground state to the first excited state. This is also the case when using the Eu^{III} structure (b-1), however, with the orientations of D1 and D2 exchanged. For Dy^{III}-5LIO, however, the orientations of the main magnetic axes do not clearly coincide with the structural features, for example, shortest bonds or symmetry axes, and non-alignment with the ground state is also observed. As is the case for Tb^{III}, the orientations of D1 and D2 of the Dy^{III} complexes are exchanged when comparing the Eu^{III}-5LIO and Gd^{III}-5LIO structures. According to Table S11, Orbach and Raman processes are likely in to occur via the first excited state for all Dy^{III} complexes. Based on these results, it was concluded that none of the complexes would show promise as single molecule magnets, and hence, their dynamic magnetic properties were not determined experimentally.

Conclusion

The ligand field effects of two very similar coordination geometries have been investigated. HF-EPR studies suggest that the ground state of the complexes is not $M_J = \pm 6$ at zero field but $M_J = \pm 4$ for Tb^{III}-2LI and $M_J = \pm 5$ for Tb^{III}-5LIO. These results agree qualitatively with the ab initio calculations, which indicate a larger ground state M_J value of the Tb^{III}-5LIO than the Tb^{III}-2LI complex. From the analysis of the EPR data we conclude that in both complexes the Tb^{III} ion has a non-axial symmetry environment. MCD spectroscopy has also been used to illustrate differences in ligand field splitting of the M_J multiplets of the ground and excited states of the two Dy^{III} complexes. The qualitative analysis of the ligand field strength is in agreement with ab initio calculations. The good agreement between ligand field theory and the pseudo spin Hamiltonian approach used in the ab initio calculations is a further important validation of the quantum chemical approach. The pseudo spin Hamiltonian used appears to give chemically reasonable parameters, making it a promising approach to determine a large number of parameters in low symmetry lanthanide complexes.

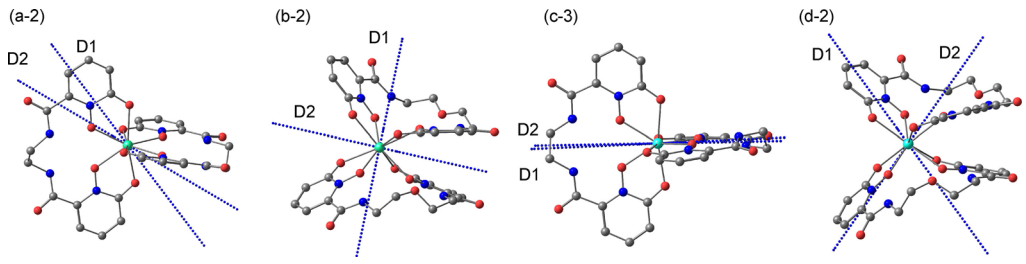

Figure 9. Orientations of the ab initio calculated main magnetic axes of the ground state doublets and first excited state doublets of (a-2) Tb^{III}-2LI, (b-2) Tb^{III}-5LIO, (c-3) Dy^{III}-2LI and (d-2) Dy^{III}-5LIO (see Table 5).

Ultimately, our aim is to determine these values by experiment but progress is slowed by a lack of an accurate way to determine MCD transition intensities to aid in assigning complex spectra. Very many more parameters are required to calculate the intensities of transitions within a multiplet rather than the integrated intensity of the transition between multiplets. We are investigating a simplified AOM approach to achieve this. Due to the high symmetry of the Ln^{III}-2LI complexes in solution, a set of similar ligands is currently in preparation. It is hoped that this new series will allow for a more comprehensive ligand field theory investigation and further validation of the ab initio methods. Nonetheless, it is apparent from this study that small differences in geometry can have a notable effect on the magnetic and electronic properties, despite the ligand field effects in lanthanide complexes being relatively weak.

Experimental Section

Measurements

Magnetic measurements: The magnetic data were collected using an MPMS-XL5 (Quantum Design) SQUID magnetometer. Fixed powder samples were prepared by pressing the powder into PTFE tape. Data were corrected for diamagnetic contributions of the sample holders and, using Pascal's constants, of the samples themselves.

High-frequency electron paramagnetic resonance (HF-EPR): Measurements of the Tb^{III} monomer complexes, that is, Tb^{III}-2LI, and Tb^{III}-5LIO, have been carried out in the frequency range of 35–300 GHz and in the temperature range of 2–60 K. A millimeter vector network analyzer (MVNA) by ABmm was used as a phase stable source and sensitive detector of microwaves for the measurements. A superconducting magnet by Oxford Instruments provides magnetic field up to 16 T, and the sample is placed in a variable temperature insert (VTI). The powder samples have been fixed by eicosane in the transmission type sample stage of the home-built EPR probe.[7b]

Magnetic circular dichroism (MCD): Spectra over a range of 9000–23000 cm^{-1} were obtained using a Jobin Yvon 750s monochromator. A Hinds photoelastic modulator was used in order to generate the circularly polarized modulation with either a Si-avalanche photodiode (visible region) or an InGaAs detector (near-IR region). Signals were acquired using Stanford SR830 lock-in amplifiers at chopped and polarized modulations to allow simultaneous measurement of absorption and MCD spectra. An Oxford SM-4 Spectramag provided the magnetic field of 5 T, in which the spectra were collected over a temperature range of 2–75 K using an Oxford ITC504 controller. The samples were prepared as 7 mM solutions in 2:1 dimethylformamide/methanol. Quartz cells of 2 mm thickness were used and quality glasses were achieved by fast cooling to around 5 K.

CCDC 1578942, 1578943, 1578944, and 1578945 contain the supplementary crystallographic data for this paper. These data are provided free of charge by The Cambridge Crystallographic Data Centre.

Elemental analyses were obtained from the microanalytical laboratory of the Chemical Institutes of the University of Heidelberg.

Ground state density functional theory (DFT) calculations

DFT geometry optimizations were performed in Gaussian 09[34] on the Baden-Württemberg HPC (bwHPC) computer cluster. The functional B3LYP was used, with the effective core potential MWB55[16] to describe Dy^{III} and 6-31G(d,p) basis sets for the remaining atoms (C, H, N, and O). An example input for the optimizations can be found in Figure S9 (Supporting Information).

Syntheses

General: Chemicals were used as supplied. The ligands 2LI- and 5LIO-1,2-HOPO were prepared as described elsewhere.[9] The syntheses of the Dy^{III} and Tb^{III} complexes followed the same procedures as published for the respective Eu^{III} complexes.[9] Negative mass spectra can be found in Figure S12.

[Tb(2LI-1,2-HOPO)$_2$]PyH·H$_2$O·2 DMF·0.5 MeOH: Yield 47%; HR-ESI-MS (−) (MeOH): 823.07717 (calculated: 823.08 [$C_{28}H_{24}N_8O_{12}Tb]^-$); elemental analysis calcd (%): C 43.77, H 4.46, N 14.22; found: C 43.53, H 4.55, N 14.47.

[Dy(2LI-1,2-HOPO)$_2$]PyH·2.5 DMF: Yield 42%; HR-ESI-MS (−) (MeOH): 828.08174 (calculated: 828.08 [$C_{28}H_{24}DyN_8O_{12}]^-$). elemental analysis calcd (%): C 44.63, H 4.39, N 14.78; found: C 44.56, H 4.66, N 14.80.

[Tb(5LIO-1,2-HOPO)$_2$]PyH: Yield 60%; HR-ESI-MS (−) (MeOH): 911.13015 (calculated: 911.13 [$C_{32}H_{32}N_8O_{14}Tb]^-$). elemental analysis calcd (%): C 44.81, H 3.86, N 12.71; found: C 44.60, H 4.09, N 12.83.

[Dy(5LIO-1,2-HOPO)$_2$]PyH·H$_2$O·0.5 DMF: Yield 53%; HR-ESI-MS (−) (MeOH): 916.13348 (calculated: 916.13 [$C_{32}H_{32}DyN_8O_{14}]^-$); elemental analysis calcd (%): C 44.05, H 4.18, N 12.68; found: C 44.05, H 4.19, N 12.82.

Acknowledgements

The Graduate School HGS MathComp of the IWR, the University of Heidelberg and the COST Action CM1305 "Explicit Control Over Spin States in Technology and Biochemistry" (ECOSTBio) are gratefully acknowledged for financial support. We also acknowledge the support by the state of Baden-Württemberg through bwHPC and the German Research Foundation (DFG) through grant no INST 40/467-1 FUGG. L.J.D. gratefully acknowledges a Feodor Lynen Fellowship of the Alexander von Humboldt foundation.

Conflict of interest

The authors declare no conflict of interest.

Keywords: ab initio calculations · magnetic circular dichroism · EPR spectroscopy · lanthanides · ligand effects · magnetic properties

[1] R. Sessoli, D. Gatteschi, A. Caneschi, M. A. Novak, *Nature* **1993**, *365*, 141–143.

[2] a) L. Bogani, W. Wernsdorfer, *Nat. Mater.* **2008**, *7*, 179–186; b) M. N. Leuenberger, D. Loss, *Nature* **2001**, *410*, 789–793; c) F. Meier, J. Levy, D. Loss, *Phys. Rev. B* **2003**, *68*, 134417; d) J. Lehmann, A. Gaita-Arino, E. Coronado, D. Loss, *Nat. Nanotechnol.* **2007**, *2*, 312–317.

[3] a) R. Sessoli, A. K. Powell, *Coord. Chem. Rev.* **2009**, *253*, 2328–2341; b) F. Neese, D. A. Pantazis, *Faraday Discuss.* **2011**, *148*, 229–238.

[4] a) F. S. Guo, B. M. Day, Y. C. Chen, M. L. Tong, A. Mansikkamaki, R. A. Layfield, *Angew. Chem. Int. Ed.* **2017**, *56*, 11445 – 11449; *Angew. Chem.* **2017**, *129*, 11603 – 11607; b) C. A. P. Goodwin, F. Ortu, D. Reta, N. F. Chilton, D. P. Mills, *Nature* **2017**, *548*, 439 – 442; c) Y. C. Chen, J. L. Liu, L. Ungur, J. Liu, Q. W. Li, L. F. Wang, Z. P. Ni, L. F. Chibotaru, X. M. Chen, M. L. Tong, *J. Am. Chem. Soc.* **2016**, *138*, 2829 – 2837.

[5] a) P. Å. Malmqvist, B. O. Roos, B. Schimmelpfennig, *Chem. Phys. Lett.* **2002**, *357*, 230 – 240; b) C. Rudowicz, *J. Phys. C* **1985**, *18*, 1415 – 1430.

[6] J. van Leusen, M. Speldrich, H. Schilder, P. Kögerler, *Coord. Chem. Rev.* **2015**, *289 – 290*, 137 – 148.

[7] a) P. Comba, M. Enders, M. Grosshauser, M. Hiller, D. Müller, H. Wadepohl, *Dalton Trans.* **2017**, *46*, 138 – 149; b) P. Comba, M. Grosshauser, R. Klingeler, C. Koo, Y. Lan, D. Müller, J. Park, A. Powell, M. J. Riley, H. Wadepohl, *Inorg. Chem.* **2015**, *54*, 11247 – 11258; c) M. Bender, P. Comba, S. Demeshko, M. Großhauser, D. Müller, H. Wadepohl, *Z. Anorg. Allg. Chem.* **2015**, *641*, 2291 – 2299.

[8] P. Comba, M. Enders, M. Großhauser, R. Klingeler, C. Koo, M. Hiller, D. Müller, G. Rajaraman, M. Tavhelidse, H. Wadepohl, *unpublished results*.

[9] a) L. J. Daumann, D. S. Tatum, C. M. Andolina, J. I. Pacold, A. D′Aleo, G.-l. Law, J. Xu, K. N. Raymond, *Inorg. Chem.* **2016**, *55*, 114 – 124; b) L. J. Daumann, D. S. Tatum, B. E. R. Snyder, C. Ni, G.-l. Law, E. I. Solomon, K. N. Raymond, *J. Am. Chem. Soc.* **2015**, *137*, 2816 – 2819.

[10] J. L. Hoard, J. V. Silverton, *Inorg. Chem.* **1963**, *2*, 235 – 242.

[11] a) E. G. Moore, J. Xu, C. J. Jocher, E. J. Werner, K. N. Raymond, *J. Am. Chem. Soc.* **2006**, *128*, 10648 – 10649; b) E. G. Moore, J. Xu, C. J. Jocher, I. Castro-Rodriguez, K. N. Raymond, *Inorg. Chem.* **2008**, *47*, 3105 – 3118.

[12] SHAPE 2.1, M. Llunell, D. Casanova, J. Cirera, P. Alemany, S. Alvarez, Barcelona, **2013**.

[13] a) M. Pinsky, D. Avnir, *Inorg. Chem.* **1998**, *37*, 5575 – 5582; b) J. Cirera, E. Ruiz, S. Alvarez, *Chem. Eur. J.* **2006**, *12*, 3162 – 3167; c) D. Casanova, J. Cirera, M. Llunell, P. Alemany, D. Avnir, S. Alvarez, *J. Am. Chem. Soc.* **2004**, *126*, 1755 – 1763; d) D. Casanova, M. Llunell, P. Alemany, S. Alvarez, *Chem. Eur. J.* **2005**, *11*, 1479 – 1494.

[14] V. S. Mironov, Y. G. Galyametdinov, A. Ceulemans, C. Görller-Walrand, K. Binnemans, *J. Chem. Phys.* **2002**, *116*, 4673 – 4685.

[15] J. D. Rinehart, J. R. Long, *Chem. Sci.* **2011**, *2*, 2078 – 2085.

[16] a) M. Dolg, H. Stoll, H. Preuss, *Theor. Chim. Acta* **1993**, *85*, 441 – 450; b) M. Dolg, H. Stoll, A. Savin, H. Preuss, *Theor. Chim. Acta* **1989**, *75*, 173 – 194.

[17] a) Z.-X. Jiang, J.-L. Liu, Y.-C. Chen, J. Liu, J.-H. Jia, M.-L. Tong, *Chem. Commun.* **2016**, *52*, 6261 – 6264; b) J. Liu, Y. C. Chen, J. L. Liu, V. Vieru, L. Ungur, J. H. Jia, L. F. Chibotaru, Y. Lan, W. Wernsdorfer, S. Gao, X. M. Chen, M. L. Tong, *J. Am. Chem. Soc.* **2016**, *138*, 5441 – 5450; c) P. Zhang, L. Zhang, C. Wang, S. Xue, S.-Y. Lin, J. Tang, *J. Am. Chem. Soc.* **2014**, *136*, 4484 – 4487; d) I. Oyarzabal, J. Ruiz, J. M. Seco, M. Evangelisti, A. Camon, E. Ruiz, D. Aravena, E. Colacio, *Chem. Eur. J.* **2014**, *20*, 14262 – 14269; e) A. V. Gavrikov, N. Efimov, Z. Dobrohotova, A. B. Ilyukhin, P. N. Vasilyev, V. M. Novotortsev, *Dalton Trans.* **2017**, *46*, 11806 – 11816; f) S. Biswas, V. S. Bejoymohandas, M. L. P. Reddy, K. S. Das, P. Kalita, M. L. P. Reddy, I. Oyarzabal, E. Colacio, V. Chandrasekhar, *Inorg. Chem.* **2017**, *56*, 7985 – 7997.

[18] P. Ma, F. Hu, R. Wan, Y. Huo, D. Zhang, J. Niu, J. Wang, *J. Mater. Chem. C* **2016**, *4*, 5424 – 5433.

[19] a) W. B. Sun, B. L. Han, P. H. Lin, H. F. Li, P. Chen, Y. M. Tian, M. Murugesu, P. F. Yan, *Dalton Trans.* **2013**, *42*, 13397 – 13403; b) J.-Y. Ge, L. Cui, J. Li, F. Yu, Y. Song, Y.-Q. Zhang, J.-L. Zuo, M. Kurmoo, *Inorg. Chem.* **2017**, *56*, 336 – 343; c) S. Xue, L. Zhao, Y. N. Guo, R. Deng, Y. Guo, J. Tang, *Dalton Trans.* **2011**, *40*, 8347 – 8352; d) B. Yao, B. Gu, M. Su, G. Li, Y. Ma, L. Li, Q. Wang, P. Cheng, X. Zhang, *RSC Adv.* **2017**, *7*, 2766 – 2772.

[20] C. Görller-Walrand, K. Binnemans, in *Handbook on the Physics and Chemistry of Rare Earths, Vol. 25* (Eds.: K. A. J. Gschneidner, L. Erying), Elsevier Science, **1998**, pp. 101 – 264.

[21] Origin (OriginLab, Northampton, MA).

[22] C. E. Schäffer, *Struct. Bonding* **1968**, *5*, 68 – 95.

[23] C. Görller-Walrand, K. Binnemans in *Handbook on the Physics and Chemistry of Rare Earths, Vol. 23* (Eds.: K. A. J. Gschneidner, L. Erying), Elsevier Science, **1996**, pp. 121 – 283.

[24] W. Urland, *Chem. Phys.* **1976**, *14*, 393 – 401.

[25] B. M. Flanagan, P. V. Bernhardt, E. R. Krausz, S. R. Luethi, M. J. Riley, *Inorg. Chem.* **2002**, *41*, 5024 – 5033.

[26] L. F. Chibotaru, L. Ungur, *J. Chem. Phys.* **2012**, *137*, 064112.

[27] R. S. Rana, J. Shertzer, F. W. Kaseta, R. Garvey, D. Rana, S. Y. Feng, *J. Chem. Phys.* **1988**, *88*, 2242 – 2248.

[28] I. D. Ryabov, *Appl. Magn. Reson.* **2009**, *35*, 481 – 494.

[29] B. O. Roos, P. R. Taylor, P. E. M. Siegbahn, *Chem. Phys.* **1980**, *48*, 157 – 173.

[30] L. Ungur, W. Van den Heuvel, L. F. Chibotaru, *New J. Chem.* **2009**, *33*, 1224 – 1230.

[31] R. D. Shannon, *Acta Crystallogr. Sect. A* **1976**, *32*, 751 – 767.

[32] A. Abragam, B. Bleaney, *Electron Paramagnetic Resonance of Transition Ions*, Oxford University Press, Oxford, UK, **1970**.

[33] M. N. Leuenberger, D. Loss, *Phys. Rev. B* **2000**, *61*, 1286 – 1302.

[34] Gaussian 09, M. J. Frisch, G. W. Trucks, H. B. Schlegel, G. E. Scuseria, M. A. Robb, J. R. Cheeseman, G. Scalmani, V. Barone, B. Mennucci, G. A. Petersson, H. Nakatsuji, M. Caricato, X. Li, H. P. Hratchian, A. F. Izmaylov, J. Bloino, G. Zheng, J. L. Sonnenberg, M. Hada, M. Ehara, K. Toyota, R. Fukuda, J. Hasegawa, M. Ishida, T. Nakajima, Y. Honda, O. Kitao, H. Nakai, T. Vreven, J. A. Montgomery, Jr., J. E. Peralta, F. Ogliaro, M. J. Bearpark, J. Heyd, E. N. Brothers, K. N. Kudin, V. N. Staroverov, R. Kobayashi, J. Normand, K. Raghavachari, A. P. Rendell, J. C. Burant, S. S. Iyengar, J. Tomasi, M. Cossi, N. Rega, N. J. Millam, M. Klene, J. E. Knox, J. B. Cross, V. Bakken, C. Adamo, J. Jaramillo, R. Gomperts, R. E. Stratmann, O. Yazyev, A. J. Austin, R. Cammi, C. Pomelli, J. W. Ochterski, R. L. Martin, K. Morokuma, V. G. Zakrzewski, G. A. Voth, P. Salvador, J. J. Dannenberg, S. Dapprich, A. D. Daniels, Ö. Farkas, J. B. Foresman, J. V. Ortiz, J. Cioslowski, D. J. Fox, Gaussian Inc., Wallington CT, **2009**.

Manuscript received: October 12, 2017
Accepted manuscript online: February 6, 2018
Version of record online: ■■ ▮▮, 0000

FULL PAPER

Correlation: Two subtly different coordination geometries are shown to induce notably different ligand field splitting of the ground and excited *J* multiplets of Tb^{III} and Dy^{III}. A combination of magnetic circular dichroism and ligand field analysis, high-frequency EPR, magnetic measurements, and ab initio calculations is used to illustrate the sensitivity of Ln^{III} ions to ligand field effects.

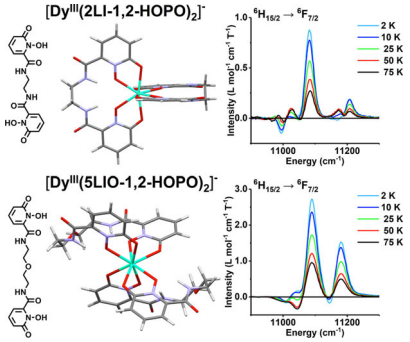

Magnetic Properties

P. Comba, L. J. Daumann, R. Klingeler, C. Koo, M. J. Riley, A. E. Roberts, H. Wadepohl, J. Werner*

■■ – ■■

Correlation of Structural and Magnetic Properties in a Set of Mononuclear Lanthanide Complexes